

PAPER



Cite this: *J. Mater. Chem. C*, 2018, 6, 2329

Received 10th December 2017,
Accepted 2nd February 2018

DOI: 10.1039/c7tc05661c

rsc.li/materials-c

Laser-driven propulsion of multilayer graphene oxide flakes†

Chengbing Qin,^{ib}*^{ab} Zhixing Qiao,^{ab} Wenjun He,^{ab} Yani Gong,^{ab} Guofeng Zhang,^{ab} Ruiyun Chen,^{ab} Yan Gao,^{ab} Liantuan Xiao*^{ab} and Suotang Jia^a

Microjet engines have attracted significant research interest due to their fascinating capabilities to pick up, transport, and release various microcargoes. Here, we show that artificially designed multilayer graphene oxide (GO) flakes on a glass surface can be propelled by femtosecond laser irradiation, which is attributed to the rapid expansion and ejection of gases during the photoreduction of the GO by a femtosecond laser. The reduction of GO was characterized by Raman spectroscopy, Fourier transform infrared spectroscopy, and X-ray photoelectron spectroscopy. The ejection of gases was confirmed by the rising pressure in a vacuum chamber. The significant propulsion of GO flakes driven by femtosecond laser irradiation provides considerable promise for the design and fabrication of practical laser-driven micromachines toward a wide range of important future applications, with the features of wireless steering, short triggering time, and lack of toxicity.

1. Introduction

After its rapid development during the last century, the jet engine has already become an indispensable part of many activities in our daily life. For example, they are used in industrial gas turbines and jet aircraft, which have also laid the foundation for the Space Age.¹ The versatile microjet engine was created with inspiration from the great advance of macroscopic machines, and this engine has also attracted significant research interest in the last decades, due to its fascinating capabilities to pick up, transport, and release various micro/nanocargoes.² Currently, the microjet engine has been used to design and build multifunctional and intelligent microscale machines that manifest great potential in the areas of drug delivery, cell separation, microsurgery, lithography, and environmental remediation.² Among many structures, tubular microengines,³ asymmetric catalytic nanorods,⁴ and spherical Janus micromotors⁵ based on bubble propulsion in the presence of hydrogen peroxide (H₂O₂) have attracted considerable attention.

A tubular microengine was first introduced in 2009 by Solovev *et al.*,⁶ who fabricated a rolled-up microtube with a platinum (Pt) inner shell as the catalytic surface. The inner layer served as a chemical reaction chamber where the fuel of H₂O₂ would be

catalyzed to produce gaseous oxygen, 2H₂O₂ → 2H₂O + O₂. The gas bubbles were ejected from one opening of the tube, resulting in a microjet engine that moved the microtube forward, propelled by the bubble recoil force. Asymmetric catalytic nanorods (dubbed rod-shaped nanoswimmers) have also been developed by generating a local product gradient through breaking down similar chemical fuels located on two sides, and creating a self-diffusiophoretic or electrophoretic flux to achieve directed motion. Taking Pt/Au nanorods as an example,⁷ the Pt side catalytically generated oxygen bubbles that emerged in H₂O₂ solution, leading to different hydrodynamic boundary conditions on the Pt side as compared to the Au side. The Janus micromotor is another important asymmetric microjet engine with a spherical shape, and it has been thoroughly investigated and designed to perform a wide variety of operations, from incorporating novel metal to amorphous titanium dioxide (am-TiO₂),⁸ to catalyzing the decomposition of H₂O₂ to the light-driven photocatalytic reaction of hydrazine,⁹ and from biomedical applications to water purification.¹⁰

All of the microjet engines mentioned above rely on the catalytic reaction of toxic fuels that are incompatible with living organisms and are harmful for environment. Additionally, these engines can only perform in solution, where strong Brownian motion will reduce the manipulations of microjet engines and cause weak direction and velocity controllability as well as long response time, resulting in limits to practical applications.¹¹ Accordingly, a microjet engine that can operate under arid conditions is therefore necessary to widen the range of applications of available micromotors so that they can be used on surfaces and in air, and to avoid the use of toxic fuels.¹¹

^a State Key Laboratory of Quantum Optics and Quantum Optics Devices, Institute of Laser Spectroscopy, Shanxi University, Taiyuan, Shanxi 030006, China. E-mail: chbqin@sxu.edu.cn, xlt@sxu.edu.cn

^b Collaborative Innovation Center of Extreme Optics, Shanxi University, Taiyuan, Shanxi 030006, China

† Electronic supplementary information (ESI) available. See DOI: 10.1039/c7tc05661c

In this work, we present a microjet engine, based on the distinct propulsion resulting from photoreduction of artificially designed multilayer graphene oxide (GO) flakes. The microjet engine moves on a dry glass substrate with a femtosecond laser as the remote driver. The propulsion is derived from the rapid ejection of gas during the photoreduction of oxygen-containing functional groups on the basal plane of the GO. This new type of GO-based microjet engine can be wirelessly and remotely controlled at will with extremely high spatial and temporal precision by regulating the “on/off” switch and the intensity of the laser, and it has potential applications in versatile micromachines.

2. Experimental

2.1 Materials

The GO suspensions (0.5 mg mL^{-1}) were purchased from Nanjing XFNANO Materials Tech Co. Ltd, and the flakes in the suspension were synthesized by modified Hummers method (the detailed process has been described in the ESI†). The original GO suspensions were slightly reduced by exposing the materials to an Hg lamp with a duration time of 10 min at power of 500 W (see Section 1 in ESI† for more detail). After reduction, $100 \mu\text{L}$ GO dispersion with concentration of $1 \times 10^{-2} \text{ mg mL}^{-1}$ was drop-coated onto a cleaned glass substrate. Then, the prepared GO sample was dried in vacuum at room temperature for 24 h to remove the remaining solvent. A femtosecond laser with the power of 2.8 W and duration of $3 \mu\text{s}$ was used to ablate the GO flakes to fabricate a gas-flow channel, through a high numerical aperture ($60\times$, $\text{NA} = 0.75$).

2.2 Characterization

The chemical components of the GO samples before and after femtosecond laser irradiation were investigated by Raman spectroscopy, Fourier transfer infrared spectroscopy (FTIR), and X-ray photoelectron spectroscopy (XPS). Raman spectra were obtained using a custom-built Raman system equipped with a 532 nm laser source and a long focus monochromator (Horiba Jobin Yvon, 1250M). The FTIR spectra were recorded on the Si substrate with a commercial Bruker FTIR spectrometer (Nicolet iS50). XPS analysis was conducted using a VG Multilab 2000 spectrometer (Thermo Electron Corporation) with Al K α irradiation as the excitation source (300 W).

2.3 Optical experiments

The experiments involved laser irradiation and fluorescence imaging of multilayer GO that were all observed with a custom-built scanning confocal microscope. The experimental setup has been described elsewhere,^{12–14} and can also be found in the ESI† (Fig. S6). Specifically, the femtosecond laser (Mai Tai DeepSee, Spectra-Physics) at the wavelength of 820 nm, pulse width of 70 femtoseconds, and maximum power of 2.8 W was used to propel the GO flakes. Here, the duration of the femtosecond laser used to irradiate the GO flakes was only $3 \mu\text{s}$ each time with power of 210 mW, except for the last time when 350 mW was used. The power of the femtosecond laser was gradually

optimized from low to high until propulsion was observed. When the power was too low (such as the power used in the experiment was less than 185 mW), no obvious propulsion was observed. However, when the power was too high (more than 350 mW), the flakes directly broke into fragments. Given that the fluorescence of the GO materials excited by the femtosecond laser was extremely weak in our detection region (Fig. S4 in the ESI† shows the fluorescence spectra), the propulsion trajectories were visualized by confocal fluorescence imaging through a 405 nm continuum-wave (CW) laser. For the fluorescence imaging, the excitation power was 0.2 mW, and the integration time for each pixel was 1 ms.

3. Results and discussion

3.1 Preparation of GO flakes and their optical imaging

In order to effectively propel the GO flakes by femtosecond laser, the sample was carefully designed. Firstly, the thick multilayer GO flakes are beneficial for laser-driven propulsion because additional gases are being ejected during photoreduction by the femtosecond laser irradiation. In the experiment, the original GO suspension was slightly reduced by Hg lamp irradiation, resulting in the re-aggregation of GO and the formation of multilayer GO flakes (the photograph and characterizations of the GO before and after Hg lamp irradiation are presented and discussed in the ESI†, Fig. S1 and S2, respectively). Secondly, it was optimal for the GO flakes to be separated from each other and form island-like structures. Hence, in the experiment, the GO sample was prepared by drop-coating the diluted GO dispersion, rather than the spin-coating method, which will form a nearly continuous film with a monolayer or few-layered GO (Fig. S3, ESI†). Thirdly, the gas-flow channel was pre-designed and fabricated to propel the GO flakes upon command. Here, the femtosecond laser with high power was used to ablate the materials and form the gas-flow channel.

Fig. 1a presents the optical image of the final GO sample drop-coated onto the glass substrate. The multilayer GO flakes have been efficiently separated from each other to form the island-like structure (see Fig. S3 in the ESI† for more detail). To obtain detailed information on these structures, Fig. 1b displays the transmission image of the dashed region highlighted in Fig. 1a, selected for the investigation of laser-driven propulsion. The lateral dimensions of these two flakes are approximately $30 \mu\text{m}$, much larger than that of the monolayer GO film (with a diameter of $1\text{--}5 \mu\text{m}^{12}$), indicating that these two GO flakes aggregated into clumps composed of many small monolayer GO films. Specifically, the upper smaller one with thicker layers (with an average thickness of approximately 216 nm) is more compactable, while the bottom larger one with less layers has many valleys, hinting that there are very few or even no GO films in some areas. Fig. 1c presents the confocal fluorescence image of the GO sample excited by a 405 nm CW laser. It can be determined that the fluorescence intensity of the upper flake is much stronger than that of the bottom one. There are two possible reasons for this phenomenon. One is that the bottom flake has fewer GO

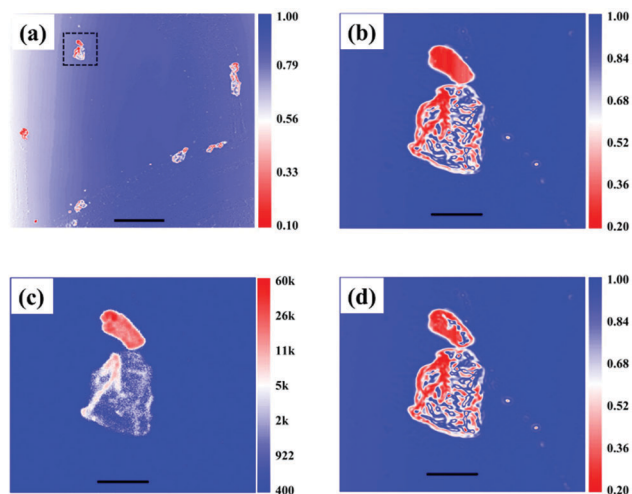


Fig. 1 Characterization of the prepared GO sample. (a) Optical image of GO drop-coated onto the cleaned glass; scale bar: 100 μm . (b) Original transmission image of a selected region that is highlighted in (a) by the dashed square. (c) Confocal fluorescence image by 405 nm CW laser with power of 0.2 mW. (d) Transmission image after femtosecond laser ablation on the selected positions with the power of 2.8 W. (b–d) Scale bar: 20 μm .

layers, such as the right part with many valleys. The other is that the oxygen-containing functional groups in the upper flake may be much more abundant as compared to the bottom one, because the boundary of the oxidized carbon atom regions has been regarded as the origin of GO's fluorescence.^{15,16} The fluorescence spectra for different areas have been recorded and are displayed in Fig. S5, ESI,[†] which are in good agreement with previous studies.¹⁷ In the experiment, the upper flake was selected to demonstrate the laser-driven propulsion. In order to propel the upper flake away from the bottom flake, the femtosecond laser with high power of 2.8 W was used to ablate the upper GO flake to form the gas-flow channel. As shown in Fig. 1d, the ablation was along the right side of the upper flake, leading to the formation of some holes or valleys. As discussed below, these holes and valleys will form the channel to eject the gases that are produced during photoreduction, resulting in the significant propulsion of the upper GO flake towards the upper-left direction.

3.2 Propulsion of GO flakes

The sequences of confocal fluorescence images for the two multilayer GO flakes after each time of femtosecond laser irradiation are presented in Fig. 2, where the ordinal numbers on the top right denote the times of irradiation. Apparently, distinct displacements between the two flakes can be observed. The upper smaller GO flake shows significant propulsion toward the upper-left direction under the laser power of 210 mW, and the geometry of the flake also exhibits sharp change, especially from the 8th to 16th irradiation. However, the bottom larger GO flake continuously remains in the center of the images, as highlighted by the yellow dashed lines. The geometry of this flake remains mostly unchanged during femtosecond laser irradiation. When increasing the power of the femtosecond

laser to 350 mW, the two flakes were directly broken, and this occurred during the 21st irradiation, as shown in Fig. 2l. To verify that the displacements were driven by the femtosecond laser rather than the CW laser (which was used to take fluorescence images), we irradiated the same flakes with a 405 nm laser using the same averaged power and duration time after each time of femtosecond laser irradiation. No obvious displacement can be observed after 30 times of irradiation (the fluorescence image arrays of CW laser irradiation between the 10th and 11th time of femtosecond laser irradiation can be found in the ESI,[†] Fig. S7). Undoubtedly, these displacements are attributed to the femtosecond laser-driven propulsion of the GO flakes.

To quantify the displacement, we defined the geometric boundary of the flakes through fluorescence thresholds, and calculated the geometric centres, named U and B for the upper and bottom ones, as shown in Fig. 3a (the detailed information associated with the calculations can be found in Section 5 of the ESI[†]). According to the scale of each pixel, the displacements of U and B were calculated and are presented in Fig. 3b and c, respectively. From the 1st to 6th irradiation, no obvious displacements occurred to either flake. Subsequently, almost linear displacements can be observed (*i.e.*, from the 7th to 17th irradiation) for the upper smaller flake, and the displacements have been up to 1 μm for each time of irradiation, even though it stopped moving the last three times of irradiation (*i.e.*, the 18th to 20th). Additionally, distinct fluorescence halos and trails can be observed opposite to the moving direction. However, for the bottom flake, no distinct displacement has occurred. More examples and movies of the propulsion of laser-driven GO flakes can be found in the ESI[†] (Fig. S12 and Videos).

Associated with the propulsion, the fluorescence intensities of both flakes are dramatically enhanced during the femtosecond laser irradiation. The averaged fluorescence intensities for the two flakes are also presented in Fig. 3b and c, respectively. The enhanced results are also induced by femtosecond laser irradiation rather than CW laser, due to no apparent changes occurring during CW laser irradiation with the same averaged power and duration time, as presented in Fig. S7, ESI.[†] During the first 10 times of irradiation, the fluorescence intensities of the upper flake are almost linearly enhanced, from 4 to 29.5. The fluorescence intensity subsequently plateaued, and then it rapidly decreased. Compared to the small flake, the fluorescence of the large flake remained unchanged during the first 12 times of irradiation, and then it is sharply enhanced. The different fluorescence variations between the upper and bottom flakes mainly resulted from the difference in their thickness.

3.3 Proposed mechanism

The mechanism interpreting both the evolution of fluorescence intensities and laser-driven propulsion of GO flakes is presented in Fig. 4. Here, we ascribe the enhanced fluorescence to the laser-induced photoreduction and the formation of quantum-dot-like GO fragments. The propulsion of the GO flake is attributed to the rapid expansion and ejection of the gases that were produced during photoreduction. In order

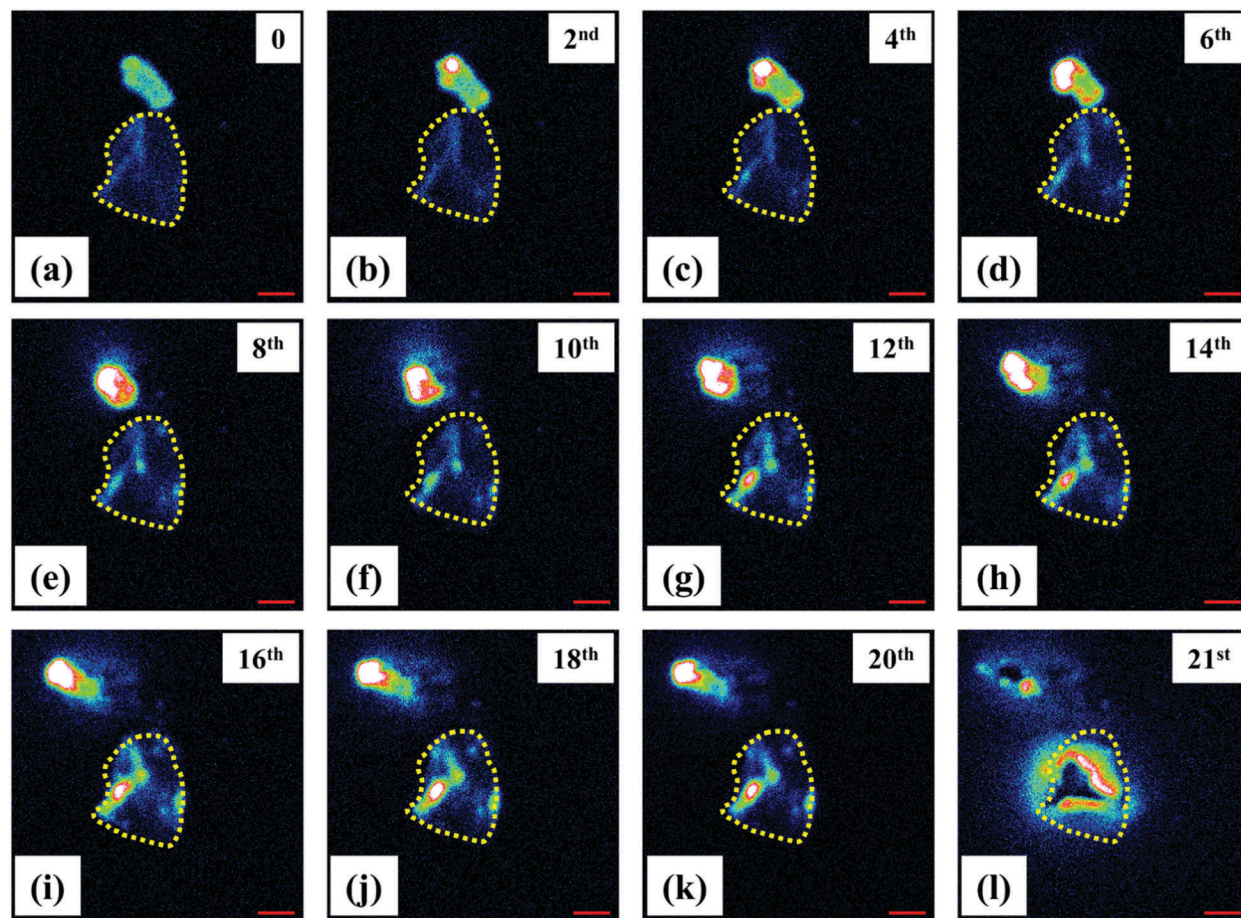


Fig. 2 Confocal fluorescence images showing the two multilayer GO flakes after femtosecond laser irradiation; the ordinal numbers on the top right denote the times of irradiation. (a) The initial fluorescence intensity without irradiation. (b–k) The fluorescence images after different times of irradiation with the power of 210 mW. (l) Fluorescence image following the 20th time of irradiation while the laser power of 350 mW is applied. The fluorescence boundary of the bottom GO flake has been highlighted by yellow dashed lines. Confocal fluorescence images were taken using a 405 nm CW laser with the power of 0.2 mW; scale bar: 10 μm .

to illustrate the experimental results, the photoreduction processes for the multilayer GO flakes are divided into three steps here.

3.3.1 First step. At the first step (*i.e.*, from the 1st to 6th irradiation for the upper flake), the femtosecond laser with high peak power will break the uppermost few layers of GO to form quantum-dot-like GO fragments.^{18,19} These fragments show strong fluorescence emission, which has also been observed by Sokolov and co-workers.²⁰ Thus, the fluorescence intensity will be dramatically enhanced, as shown in Fig. 3b for the first 6 times of irradiation of the upper flake. The femtosecond laser will simultaneously reduce the oxygen-containing functional groups and produce gases (such as H_2O , CO_2 , and CO). At this step, the produced gases are most likely to eject from the upper space, as illustrated in Fig. 4b. Therefore, the recoil force is perpendicular to the glass substrate, and no significant displacement can be observed. Additionally, the newly formed quantum-dot-like GO fragments will load at the surface of the uppermost few layers, and no distinct fluorescence halos and trails can be observed.

3.3.2 Second step. At the second step, the femtosecond laser will continue to reduce and break the deeper layer of GO, as shown

in Fig. 4c. The pre-formed GO fragments on the uppermost layers will be broken into even smaller fragments, which will quench the fluorescence, as observed by the Kuno group.¹⁹ The newly formed quantum-dot-like fragments continue to strongly emit fluorescence, which will enhance the fluorescence intensity. Thus, the competition between these two processes will increase. As shown in Fig. 3b, from the 6th to 10th irradiation, the fluorescence continues to be enhanced. However, from the 11th to 19th, the fluorescence intensity is almost maintained at a plateau level, indicating that a balance between the two processes has been established. The even smaller fragments on the uppermost layers form a densification layer, which will prevent the gases from being released from the upper space. As a consequence, there is a dire need for a new channel that will be used to eject produced gases.

In the experiment, this channel is artificially designed by using the femtosecond laser with high power to ablate the flake and change the morphology, layer thickness, and the chemical components of GO around the flake. The deep valleys formed by the ablation of a surrounding wall are used as channels for the ejecting gases, as presented in Fig. 1d. In this case, the recoiling force arising from the ejecting gases will overcome the

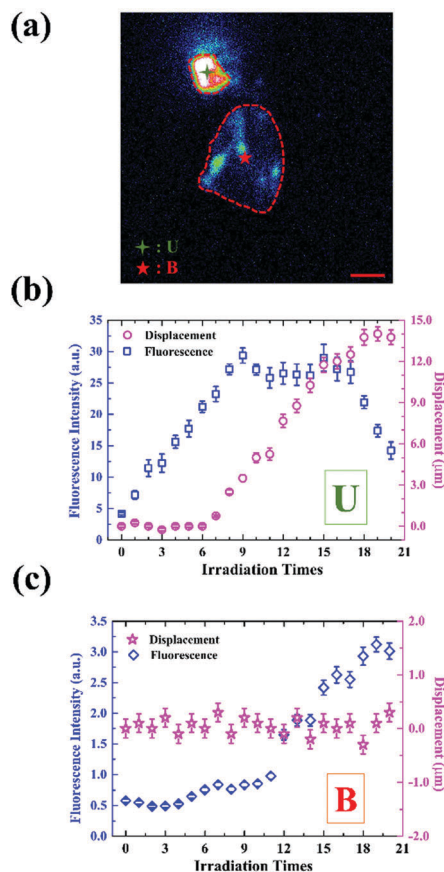


Fig. 3 The displacements and fluorescence intensities varied with laser irradiation times. (a) The boundaries of two multilayer GO flakes have been highlighted by dashed lines, according to the threshold values for fluorescence intensities, and the geometric centres have been marked as U and B for the upper and lower GO flakes, respectively. Scale bar: 10 μm. (b and c) The averaged displacements and fluorescence intensities for the U and B flakes varied with femtosecond laser irradiation.

friction between the GO and the glass substrate and propel the flake into motion. Furthermore, the newly formed quantum-dot-like GO fragments will be either follow the gas jet or recoil in the opposite direction, as illustrated in Fig. 4d, resulting in fluorescence halos and trails around the flake, as shown in Fig. 2e–k. During this step, the well-oxidized GO flakes with strong fluorescence will produce much more gases, leading to the strong recoiling force and large displacements. As a consequence, the upper thick GO flake with strong fluorescence will undergo significant propulsion, while the bottom thin flake with weak fluorescence shows no obvious changes.

3.3.3 Third step. After the deepest GO layer (or the layer that made contact with the substrate) had been reduced and broken by the femtosecond laser, the quantum-dot-like fragments decreased, resulting in fluorescence quenching, as shown in Fig. 3b for the 18th–20th irradiation. Due to the decay or even disappearance of produced gases, the flake stopped moving.

3.4 Gas ejection from bulk GO materials

Here, further evidence for the rapid ejection of gases from GO flakes has been provided by measuring the rising pressure in a

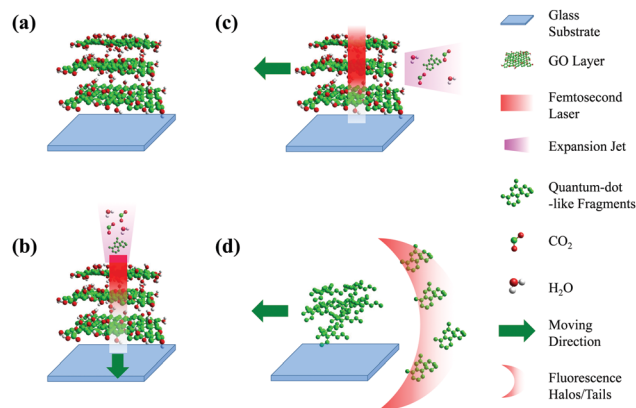


Fig. 4 Schematic representation of the laser-driven propulsion of multilayer GO flakes. (a) The prepared GO sample with many layers stacking together. (b) A few uppermost layers of GO underwent photo-reduction and produced gases that ejected from the upper space. (c) The intermediate layers underwent photoreduction and produced gases that ejected from the side edge, leading to propulsion of the GO flake. (d) The formation of fluorescence halos and tails during the propulsion of the GO flake.

vacuum chamber during femtosecond laser irradiation. A 2 mL GO suspension with the concentration of 0.5 mg mL^{−1} was drop-cast onto a cleaned and dry glass substrate. The sample was heated to 323 K in a drying box for 1 h to desorb water vapour and the remaining solvent. The process was repeated 10 times. Measurements were taken in a small chamber (approximately 150 mL volume) with a vacuum of approximately 1×10^{-2} Pa. Fig. 5 presents the variation in the chamber pressure with the times and powers of irradiation, and shows that the chamber pressure immediately increases as the laser irradiation is applied to the GO sample. For low power (2.0 W), the increase in pressure is observed to be linear with the irradiation times, indicating that persistent gases are produced during laser irradiation. Nevertheless, under high power (2.8 W), the pressure reaches the maximum value after six times of irradiation, and then it is maintained, indicating that the GO had been completely reduced and no more gases were produced.

By filling the chamber with pure nitrogen (approximately 400 Torr), the determination of producing species by quartz enhanced photoacoustic spectroscopy (QEPAS) was performed. By comparing the QEPAS signal with and without femtosecond

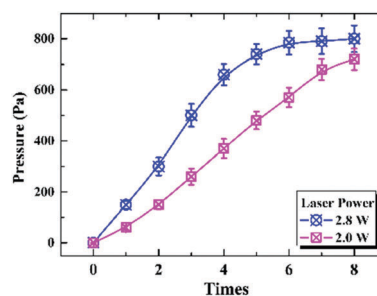


Fig. 5 The pressure of produced gases varied with the times and powers of femtosecond laser irradiation.

laser irradiation (Fig. S13, ESI[†]), both H₂O and CO₂ were clearly confirmed. Other products were also analysed by gas chromatography-mass spectrometry (GC-MS). However, the exact chemical structures for the products are still under analysis (see Section 7 in the ESI[†] for more detail).

3.5 Characterization after femtosecond laser irradiation

To systematically explore the photoreduction of GO flakes, Raman, FTIR, and XPS were adopted for sample characterization before and after femtosecond laser irradiation. As shown in Fig. 6a, two main peaks in the Raman spectra at 1336 and 1586 cm⁻¹ are assigned to D and G bands, corresponding to ordered sp²-bonded carbon and disordered sp³ bonds in the C-C bonds, respectively. The intensity ratio of the D to G band (I_D/I_G) can be used to denote the disorder degree and averaged size of the sp² fragments.^{21,22} The I_D/I_G value increasing from 1.75 to 2.06 after irradiation can be explained by the presence of smaller but more numerous sp² fragments and the removal of oxygen-containing functional groups. The crystalline size of the sp² fragments can be estimated according to the empirical Tuinstra-Koenig relationship L_a (nm) = $C/(I_D/I_G)$, where C is constant.²³ It can be concluded that the sp² size was reduced from 2.5 to 2.1 nm,²² which is consistent with the formation of quantum-dot-like fragments after femtosecond laser irradiation.

FTIR was performed to further elucidate the removal of oxygen functionalities from the reduced GO. As shown in Fig. 6b, the band between 2800–3600 cm⁻¹ is attributed to the O–H stretching vibration arising from hydroxyl groups, the bands at 1730, 1620, and 1050 cm⁻¹ can be described as the stretching modes of the C=O, C=C, and C–O groups, respectively, and the peaks located at 1420 and 1200 cm⁻¹ are assigned to the bending vibration of C–OH groups as well as the C–O asymmetric stretching vibration of an epoxy group,^{24,25} respectively. The decrease or even disappearance of hydroxyl, epoxy, and carbonyl groups strongly indicates that reduction occurred during laser

irradiation. Here, we also used XPS to quantify the degree of reduction. The C/O ratio can be calculated from the atomic percentages obtained from the survey XPS spectra, as shown in Fig. 6c. The C/O ratio increased from 2.30 to 4.09 after femtosecond laser irradiation, revealing the reduction of oxygen-containing functional groups from the GO basal plane.²² Fig. 6d presents the C1s deconvolution spectra of GO before and after irradiation. The spectra can be curve-fitted into four peak components with binding energy at approximately 284.8, 287.0, 287.9, and 290.2 eV, corresponding to the C=C/C–C, C–O (hydroxyl and epoxy), C=O (carbonyl), and O=C–O (carboxyl) species, respectively.²⁶ The results reveal the increase and broadening of the sp² carbon peak, which was due to the removal of functional groups and the formation of small quantum-dot fragments.

Atomic force microscopy (AFM) and scanning electron microscopy (SEM) with energy dispersive X-ray spectroscopy (EDS) were also performed to reveal the variation of oxygen functional groups before and after femtosecond laser irradiation. AFM shows that the thickness of the monolayer GO decreased from 1.5 nm to 1.1 nm (Fig. S15, ESI[†]) after irradiation, indicating the reduction of oxygen functional groups. According to the EDS analysis, the relative atomic content of elemental O decreased from 24.30% to 14.76%, which further indicates the presence of oxygen-containing functional groups and their reduction after femtosecond laser irradiation (see Section 8 in the ESI[†] for more detail).

Designing and building new and powerful microscale motors and propulsion modes is a critical step toward the future of intelligent microvehicles and micromachines. It is essential to precisely control the speed and direction of artificial nanomotors so that they can accurately perform various tasks and diverse applications.¹¹ The controllability of the microjet engine based on the photoreduction of GO can be realized by designing the geometric shape of multilayer GO flakes and optimizing laser irradiation parameters, respectively. In this work, the geometry of multilayer GO flakes was created by the re-aggregation of a slightly reduced GO suspension. The specific and uniform geometric shape with desired gas-flow channels may be achieved by further self-assembly approaches.^{27,28}

As previously described in this study, a femtosecond laser with an extremely high power density can also be used as an ablation laser to design gas-flow channels. Moreover, although the CW laser cannot effectively propel the GO flakes due to the slow gas production and weak recoiling force, it can be used to reduce GO to form a compact film. However, by optimizing the irradiation power and duration time of the femtosecond laser,²⁹ the direction of a GO-based microjet engine can be also controlled as required. Beyond a new type of microjet engine, GO can be used as the fuel to fill a shaped nanostructure as well, such as microtubules with a high-transmission shell or a turbine-like micro-rotor,³⁰ to power these micromachines through laser irradiation with a remote control. Although some fragments may accumulate in the micromachines, this problem can be solved by ultrasonic treatment. Furthermore, using higher oxidation GO with many oxygen-containing functional

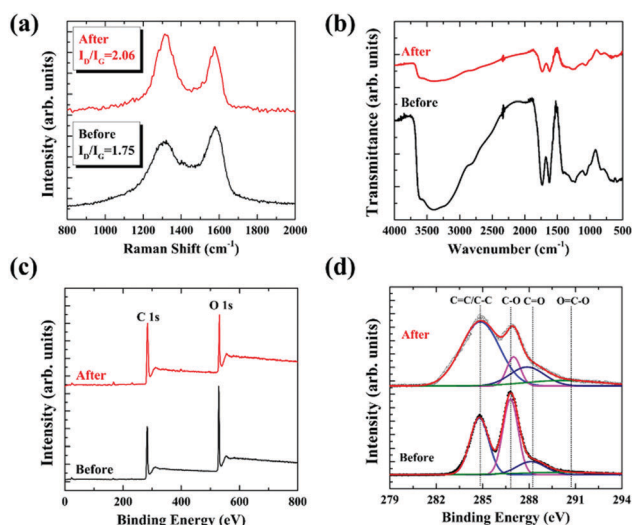


Fig. 6 Sample characterizations before and after femtosecond laser irradiation. (a) Raman spectra. (b) FTIR absorption spectra. (c) XPS survey spectra of a GO sample. (d) C1s XPS spectra of a GO sample.

groups may produce a greater quantity of gases during the photoreduction, and more effectively propel the GO flakes.

4. Conclusions

In this work, we present the propulsion of a laser-driven GO-based microjet engine that can be efficiently powered by femtosecond laser irradiation within an extremely short time (3 μ s). The propulsion originates from the rapid gas expansion and ejection of GO flakes during the photoreduction of oxygen-containing functional groups. This new type of GO-based microjet can be fabricated by drop-casting a GO dispersion onto a glass substrate and artificially designing gas-flow channels by femtosecond laser ablation. Compared to traditional micro-motors performing in aqueous solution using toxic H₂O₂ as the fuel, the GO-based microjet uses no toxic materials and can operate on a dry glass surface. The laser-driven process also allows us to power the microjet with wireless steering, fast triggering response, and precise motion control. This new type of microjet holds considerable promise for the design and fabrication of practical light-driven micromachines with a wide range of important future applications ranging from microelectromechanical systems (MEMS) to versatile microrobotic devices.

Conflicts of interest

There are no conflicts of interest to declare.

Acknowledgements

The project is sponsored by the National Key Research and Development Program of China (No. 2017YFA0304203), the National Natural Science Foundation of China (Grant No. 11434007), the National Science Foundation of China (No. U1510133, 11404200, 61527824, 11374196, and 61605104), the PCSIRT (No. IRT13076), and 1331KSC. We are indebted to Prof. Lei Dong and Dr Xukun Yin for assistance with QEPAS measurement, Dr Yifei Ma for SEM, and Jin Ren for GC-MS, respectively.

Notes and references

- J. Li, I. Rozen and J. Wang, *ACS Nano*, 2016, **10**, 5619–5634.
- M. Guix, C. C. Mayorga-Martinez and A. Merkoci, *Chem. Rev.*, 2014, **114**, 6285–6322.
- Y. Mei, A. A. Solovev, S. Sanchez and O. G. Schmidt, *Chem. Soc. Rev.*, 2011, **40**, 2109–2119.
- B. Dai, J. Wang, Z. Xiong, X. Zhan, W. Dai, C. C. Li, S. P. Feng and J. Tang, *Nat. Nanotechnol.*, 2016, **11**, 1087–1092.
- W. Gao, M. D'Agostino, V. Garcia-Gradilla, J. Orozco and J. Wang, *Small*, 2013, **9**, 467–471.
- A. A. Solovev, Y. Mei, E. Bermudez Urena, G. Huang and O. G. Schmidt, *Small*, 2009, **5**, 1688–1692.
- W. F. Paxton, K. C. Kistler, C. C. Olmeda, A. Sen, S. K. St Angelo, Y. Y. Cao, T. E. Mallouk, P. E. Lammert and V. H. Crespi, *J. Am. Chem. Soc.*, 2004, **126**, 13424–13431.
- Y. Li, F. Mou, C. Chen, M. You, Y. Yin, L. Xu and J. Guan, *RSC Adv.*, 2016, **6**, 10697–10703.
- W. Gao, A. Pei, R. Dong and J. Wang, *J. Am. Chem. Soc.*, 2014, **136**, 2276–2279.
- B. Jurado-Sanchez, S. Sattayasamitsathit, W. Gao, L. Santos, Y. Fedorak, V. V. Singh, J. Orozco, M. Galarnyk and J. Wang, *Small*, 2015, **11**, 499–506.
- J. Wang and K. M. Manesh, *Small*, 2010, **6**, 338–345.
- Y. Gao, C. Qin, Z. Qiao, B. Wang, W. Li, G. Zhang, R. Chen, L. Xiao and S. Jia, *Carbon*, 2015, **93**, 843–850.
- Y. Gao, C. Qin, Z. Qiao, B. Wang, W. Li, G. Zhang, R. Chen, L. Xiao and S. Jia, *Appl. Phys. Lett.*, 2015, **106**, 131103.
- W. He, C. Qin, Z. Qiao, G. Zhang, L. Xiao and S. Jia, *Carbon*, 2016, **109**, 264–268.
- K. P. Loh, Q. Bao, G. Eda and M. Chhowalla, *Nat. Chem.*, 2010, **2**, 1015–1024.
- J. Shang, L. Ma, J. Li, W. Ai, T. Yu and G. G. Gurzadyan, *Sci. Rep.*, 2012, **2**, 792.
- G. Eda, Y. Y. Lin, C. Mattevi, H. Yamaguchi, H. A. Chen, I. S. Chen, C. W. Chen and M. Chhowalla, *Adv. Mater.*, 2010, **22**, 505–509.
- P. Russo, R. Liang, E. Jabari, E. Marzbanrad, E. Toyserkani and Y. N. Zhou, *Nanoscale*, 2016, **8**, 8863–8877.
- M. P. McDonald, A. Eltom, F. Vietmeyer, J. Thapa, Y. V. Morozov, D. A. Sokolov, J. H. Hodak, K. Vinodgopal, P. V. Kamat and M. Kuno, *Nano Lett.*, 2013, **13**, 5777–5784.
- D. A. Sokolov, Y. V. Morozov, M. P. McDonald, F. Vietmeyer, J. H. Hodak and M. Kuno, *Nano Lett.*, 2014, **14**, 3172–3179.
- F. Liu, H. D. Ha, D. J. Han and T. S. Seo, *Small*, 2013, **9**, 3410–3414.
- J. Chen, B. Yao, C. Li and G. Shi, *Carbon*, 2013, **64**, 225–229.
- F. Tuinstra and J. L. Koenig, *J. Chem. Phys.*, 1970, **53**, 1126–1130.
- V. Le Borgne, H. Bazi, T. Hayashi, Y. A. Kim, M. Endo and M. A. El Khakani, *Carbon*, 2014, **77**, 857–867.
- H. Feng, R. Cheng, X. Zhao, X. Duan and J. Li, *Nat. Commun.*, 2013, **4**, 1539.
- Q. Zhang, H. Zheng, Z. Geng, S. Jiang, J. Ge, K. Fan, S. Duan, Y. Chen, X. Wang and Y. Luo, *J. Am. Chem. Soc.*, 2013, **135**, 12468–12474.
- D. Joung, A. Nemilentsau, K. Agarwal, C. Dai, C. Liu, Q. Su, J. Li, T. Low, S. J. Koester and J. H. Cho, *Nano Lett.*, 2017, **17**, 1987–1994.
- D. Joung, T. Gu and J. H. Cho, *ACS Nano*, 2016, **10**, 9586–9594.
- H. Fatt Teoh, Y. Tao, E. Soon Tok, G. Wei Ho and C. Haur Sow, *J. Appl. Phys.*, 2012, **112**, 064309.
- X.-F. Lin, G.-Q. Hu, Q.-D. Chen, L.-G. Niu, Q.-S. Li, A. Ostendorf and H.-B. Sun, *Appl. Phys. Lett.*, 2012, **101**, 113901.